Boosting energy storage and electrocatalytic performances by synergizing CoMoO$_4$@MoZn$_{22}$ core-shell structures

Hengqi Liu[a], Depeng Zhao[a], Ying Liu[a], Pengfei Hu[a], Xiang Wu[a,*], Hui Xia[b,*]

[a] School of Materials Science and Engineering, Shenyang University of Technology, Shenyang 110870, PR China
[b] School of Materials Science and Engineering, Nanjing University of Science and Technology, Nanjing 210094, PR China

HIGHLIGHTS

- A kind of novel CoMoO$_4$@MoZn$_{22}$ structures were directly grown on Ni foam through a two-step hydrothermal strategy.
- An as-assembled asymmetric supercapacitor keeps excellent capacitance retention after 10,000 cycles.
- The as-synthesized products present a low overpotential of 240 mV at 20 mA cm^{-2} for OER.

ARTICLE INFO

ABSTRACT

In this work, we report CoMoO$_4$@MoZn$_{22}$ core-shell structures grown on Ni foam via a simple hydrothermal route. The as-prepared products can be utilized directly as electrode materials for supercapacitors, demonstrating a capacity of 923 C g^{-1}. The as-assembled hybrid capacitor using CoMoO$_4$@MoZn$_{22}$ as positive electrode delivers an energy density of 129 Wh kg^{-1} at a power density of 2740 W kg^{-1} and a capacitance retention of 97% after 10,000 cycles. Moreover, the as-obtained products are also used as the alternative electrocatalysts, which shows a low overpotential of 240 mV at 20 mA cm^{-2} for oxygen evolution reaction (OER). It suggests that the bi-functional CoMoO$_4$@MoZn$_{22}$ structures could be potential candidate materials for future energy storage devices and electrocatalysts.

1. Introduction

Rapid development of industrial civilization and economic society has caused an increasing demand for energy sources that expected to double by 2050 [1]. Therefore, it is very urgent to design and develop some renewable and sustainable clean energy source systems. Among various energy storage devices, supercapacitors are the best examples, which possess high power density, excellent cycle stability and fast charge/discharge capability [2–6]. The performances of supercapacitor depend seriously on the morphologies and structures of their electrode materials [7–10]. Therefore, it is especially important to design electrode materials with unique spatial structure feature. Thereinto, ternary transition metal oxides have been research focuses owing to their highly active redox reaction, large specific surface area and distinct crystalline characteristics [11–13]. CoMoO$_4$ stands out due to its high theoretical capacity. However, as the electrode materials for supercapacitor, it behaves poor conductivity and cycle stabilities. In literature, several different morphologies of CoMoO$_4$ structures are reported,

such as microspheres, nanowire arrays and 3D nanosheets [14–16]. However, the supercapacitors based on single electrode materials still suffer from low energy density, unsatisfactory specific capacitance and poor cycling life, which limit their further industrial applications [17–19]. Therefore, to design novel composite electrodes have attracted considerable interests due to their synergistic effects between different electrode materials.

Recently, some alloys as emerging electrode materials have also attracted one's concerns. Ultrathin surface of the alloy is believed to be responsible for the performance improvement [20]. Xu et al. synthesized sponge-like nanoporous nickel alloy structures with capacitance of 498 C g^{-1} at a current density of 1 A g^{-1} and 95.7% retention even after 10,000 charge/discharge cycles at 40 A g^{-1} [21]. Wu's group reported Ni-Co alloys showing a specific capacitance of 240 C g^{-1} [22]. Li and coworkers prepared Ni-B alloys exhibiting a specific capacitance of 1003 C g^{-1} at 1 A g^{-1} [23].

Electrochemical water splitting for oxygen evolution reaction (OER) can convert electrical energy to chemical energy, which are one of the

---

* Corresponding authors.
  E-mail addresses: wuxiang05@sut.edu.cn (X. Wu), xiahui@njust.edu.cn (H. Xia).

most clean energy and efficient carriers [24]. However, it presents a high overpotential and sluggish kinetic process. Therefore, in order to overcome these drawbacks, it is important to precisely design and rationally synthesize novel catalysts for improving half reaction rate [25,26]. Precious metals such as ruthenium (Ru) and iridium (Ir) oxides exhibit excellent OER performance, but their high cost and scarcity have seriously limited their widespread applications [27–29]. Therefore, it is indispensable to fabricate cheap, earth-abundant catalysts. Transition metal oxides are considered ideal alternatives. Among them, $CoMoO_4$-based catalysts have attracted enormous interest owing to the prominent redox activities and modest overpotential under mild reaction conditions [30–32]. For example, $CoMoO_4$ nanorods grown on Ni foam showed an overpotential of 343 mV at 10 mA cm^{-2} [33]. $CoMoO_4$ porous nanoflowers as the electrocatalysts for OER exhibited electrocatalytic performance of 312 mV at 10 mA cm^{-2} [34]. However, their catalytic activities are still inferior to precious metal oxides. Heterogeneous electrocatalysts can accelerate electrochemical reactions on the surface of electrode materials. At the same time, surface and interface engineering could obtain novel physical and chemical properties and excellent synergistic effects in heterogeneous electrocatalysts [35,36]. Thus, to develop highly active heterostructured electrocatalysts is an important task.

In this work, we report a kind of novel $CoMoO_4@MoZn_{22}$ structures directly grown on Ni foam through a facile hydrothermal strategy. The as-synthesized products consist of $CoMoO_4$ nanosheets as the cores and $MoZn_{22}$ nanofilms as the shells with excellent conductivity. Hybrid $CoMoO_4@MoZn_{22}$ structures as the electrode materials show a high capacitance of 923 C g^{-1} at a current density of 1 A g^{-1}. An as-assembled asymmetric supercapacitor keeps 97% capacitance retention after 10,000 cycles at current density of 4 A g^{-1}. Meanwhile, owing to sheet-like structure feature, the as-synthesized products present a low overpotential of 240 mV at 20 mA cm^{-2} for OER in 1 M KOH.

2. Experimental section

In the experiments, all chemicals were used as received without further purification. Prior to the synthesis, Ni foam (2 × 2 cm^2) was immersed into 3 M HCl solution for 30 min to remove the oxidation film and grease on the surface. Next, Ni foam was cleaned by sonication in deionized water and ethanol in sequence for 30 min and then dried overnight.

2.1. Synthesis of $CoMoO_4$ nanosheets

$CoMoO_4$ nanosheets were grown on Ni foam substrate by a facile hydrothermal method. 1 mmol Co(NO$_3$)$_2$·6H$_2$O, 1 mmol Na$_2$MoO$_4$·2H$_2$O, 5 mmol urea and 5 mmol NH$_4$F were dissolved in 40 ml deionized water and then the above solution was magnetically stirred for 30 min. After that, the uniform solution was transferred into a 100 ml autoclave. Afterwards, a piece of pre-treated Ni foam was immersed into it. The autoclave was heated at 140 °C for 6 h. After cooled to room temperature, Ni foam was taken out and washed with ethanol and deionized water three times, respectively. The prepared sample was dried at 60 °C for 12 h, followed by calcination at 300 °C for 2 h. The average mass loading of Ni foam is 1.0 mg cm^{-2}.

2.2. Synthesis of $CoMoO_4@MoZn_{22}$ nanosheets

To synthesize $CoMoO_4@MoZn_{22}$ samples, a hydrothermal method was utilized for the growth of $MoZn_{22}$ on the precursors of $CoMoO_4$. The Ni foam coating $CoMoO_4$ precursors was put into a 100 ml autoclave with the solution of 2 mmol Zn (NO$_3$)$_2$·6H$_2$O, 2 mmol Na$_2$MoO$_4$·2H$_2$O. After continuous stirring for 30 min, the autoclave was heated at 140 °C for 7 h. The treat process was the same as the above experiments. Average mass loading of Ni foam is 2.1 mg cm^{-2}.

2.3. Material characterization

The composition and crystal structure of the as-synthesized samples were measured by a powder X-ray diffraction analyzer (XRD, Shimadzu-7000) with Cu Kα radiation (λ = 0.1541 nm, 40 KV). X-ray photoelectron spectra (XPS) measurements (ESCALAB250) were conducted to investigate the elemental composition and surface states using an Al Kα source. The structure and morphology of the samples were characterized by using a scanning electron microscope (SEM, Gemini, 300-71-31) and a high resolution transmission electron microscope (HRTEM, JEM-2100 PLUS) operated at 200 kV.

2.4. Electrochemical measurements

Electrochemical characteristics of the as-synthesized products were studied by using a CHI660E electrochemical workstation in a standard three-electrode system. The samples were used as working electrode, Pt foil as counter electrode and Hg/HgO as reference one in 3 M KOH electrolytes. Specific capacitance of the electrode materials were calculated by the GCD curves using the follow equation:

$$Cs = I\Delta t/m \tag{1}$$

where I is current density, $\triangle$t represents discharge time and m stands for mass of the electrode.

2.5. Assembly of asymmetric supercapacitor

An asymmetric supercapacitor was constructed by using $CoMoO_4@MoZn_{22}$ sample as cathode and activated carbon (AC) as anode. The mass ratio of cathode and anode was determined to keep the charge balance by the following equations:

$$q^+ = q^- \tag{2}$$

$$q = cm\Delta V \tag{3}$$

$$m^+/m^- = C^-V^-/C^+V^+ \tag{4}$$

In the above formula, q represents charge, c is capacity, m refers the mass of the active material and V denotes voltage window.

Energy density (E) and power density (P) of the asymmetric supercapacitor can be calculated by the equations below:

$$E = 1/2CV^2 \tag{5}$$

$$P = 3600E/t \tag{6}$$

2.6. Electrocatalytic activity

In the experiment, Ag/AgCl was used as the reference electrode in the electrolyte of 1 M KOH. All potentials were measured by the equation: $E_{RHE} = E_{Ag/AgCl} + 0.197 V + 0.059 V \times pH$ (1.0 M KOH, pH ~13.6) [37]. The overpotential was calculated using the equation: $\eta = E_{RHE} - 1.23 V$. Linear sweep voltammetry (LSV) polarization curves, EIS, double-layer capacitance (C_{dl}), long-term durability were investigated in detailed in order to evaluate OER performance of the as-synthesized products.

3. Results and discussion

$CoMoO_4@MoZn_{22}$ samples are synthesized through a hydrothermal method, as illustrated in Fig. 1. Pristine $CoMoO_4$ nanosheets are grown on Ni foam first. Secondly, $MoZn_{22}$ nanofilms are covered on the surface of $CoMoO_4$ precursors by second hydrothermal route and the annealing process.

The crystal structures of the as-synthesized samples are studied by XRD. Typical XRD patterns of $CoMoO_4$, $MoZn_{22}$ and $CoMoO_4@MoZn_{22}$ products are recorded and shown in Fig. 2a, which peaks marked with
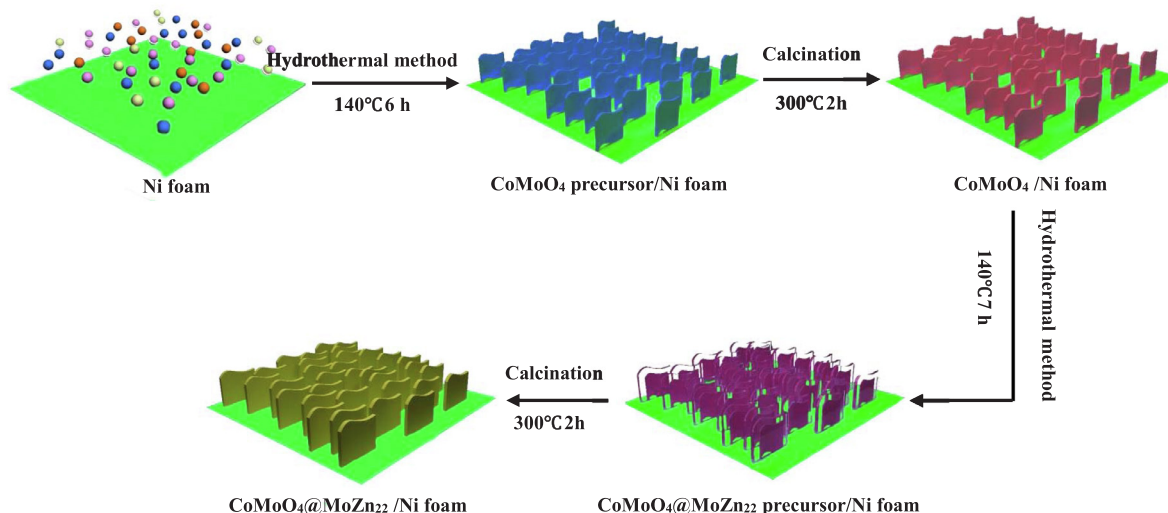
Fig. 1. Synthesis schematic illustration of CoMoO$_4$@MoZn$_{22}$/Ni foam heterostructures.

"★" are from Ni foam. XRD pattern of CoMoO$_4$ sample is marked with a red line. The diffraction peaks at 2θ of 26.5, 29.1, 33.7, 38.9 and 54.5 can be indexed to the (0 0 2), (3 1 0), (2 2 2), (0 4 0) and (4 4 0) planes of cubic phase (PDF No. 21-0868), respectively. The crystal planes of (0 3 2), (2 1 2), (1 2 3), (4 1 0) and (1 0 6) can be indexed to MoZn$_{22}$ phase (PDF No. 21-0577). Additionally, The intensity of diffraction peak of CoMoO$_4$@MoZn$_{22}$ at 2θ = 33.8° shows an increase due to the peak overlapping of CoMoO$_4$ and MoZn$_{22}$, revealing that MoZn$_{22}$ samples are successfully coated on the surface of CoMoO$_4$ precursors.

The elemental composition and surface chemical states of the as-synthesized samples were studied by XPS. In Fig. 2b, a XPS full survey spectrum of CoMoO$_4$@MoZn$_{22}$ sample is showed, indicating the presence of Co, Mo, Zn and O elements. As shown in Fig. 2c, two strong peaks at 780.5 and 796.7 eV correspond to Co 2p$_{1/2}$ and Co 2p$_{3/2}$. The

spin-orbit splitting energy between two Co 2p peaks is 16.2 eV, revealing the formation of CoMoO$_4$ product. In addition, the above mentioned peaks could be ascribed to Co^{2+} species and the peaks at 784.9 and 804.1 eV could be attributed to a charge transfer satellite. Mo 3d peaks are shown in Fig. 2d, two main peaks at 232.2 and 235.5 eV with spin orbit splitting of 3.3 eV are in accordance with the reported peaks for Mo^{6+} [38]. The Zn 2p spectrum is presented in Fig. 2e, in which two strong peaks at 1022.1 and 1044.7 eV correspond to the binding energy of Zn 2p$_{3/2}$ and Zn 2p$_{1/2}$, respectively, indicating the presence of Zn element [39]. O1s peaks at 529.8 and 531.2 eV are shown in Fig. 2f (name O1 and O3). O1 component could be attributed to metal oxygen bonds, the O3 component origins from physicochemical water at the surface of active material.

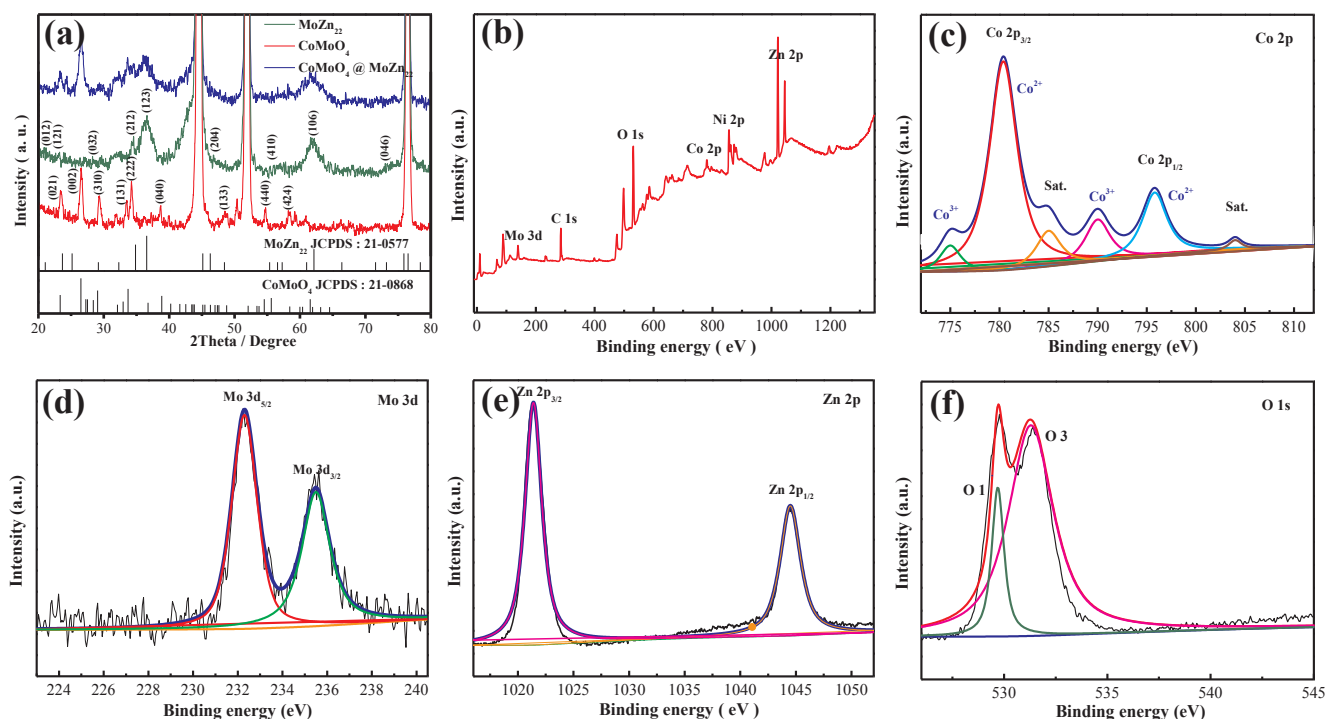Morphologies of the as-synthesized samples are observed using SEM

Fig. 2. (a) XRD patterns of CoMoO$_4$, MoZn$_{22}$ and CoMoO$_4$@MoZn$_{22}$ composites and XPS spectra of CoMoO$_4$@MoZn$_{22}$ composites (b) full spectrum (c) Co 2p (d) Mo 3d, (e) Zn 2p and (f) O 1s.
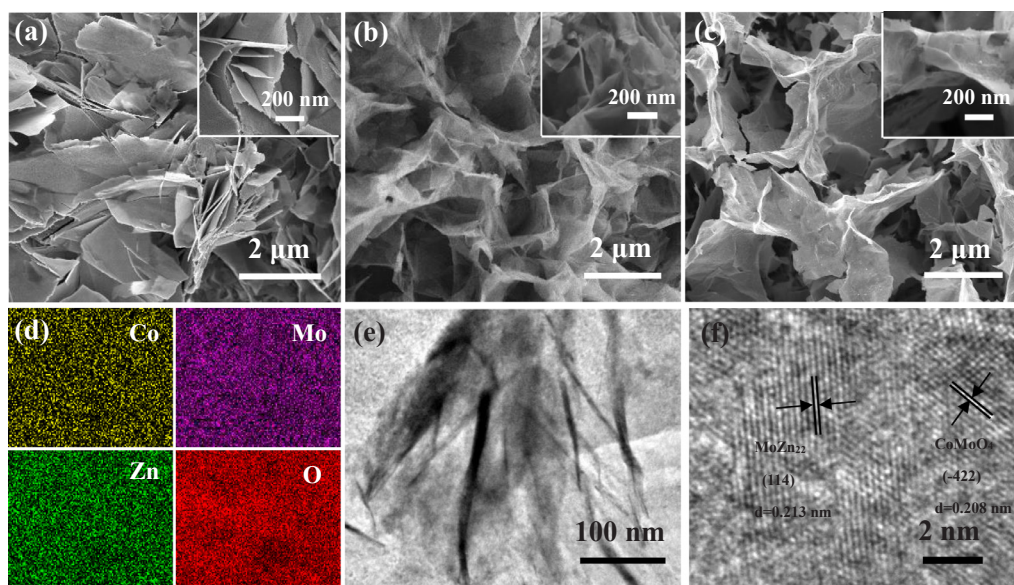
Fig. 3. (a–c) SEM images of CoMoO$_4$ nanosheets structure, MoZn$_{22}$ nanofilms and CoMoO$_4$@MoZn$_{22}$ core-shell heterostructures, the inset is the local images (d) Elemental mappings of Co, Mo, Zn and O elements (e–f) TEM images of CoMoO$_4$@MoZn$_{22}$ structure.

firstly. The as-prepared CoMoO$_4$ samples present sheet-like shape, which are uniformly covered on the whole surface of Ni foam with small pores. The average thickness of the nanosheets is around 10 nm, as shown in inset in Fig. 3a. SEM image of the as-prepared MoZn$_{22}$ samples (Fig. 3b) shows film morphology. CoMoO$_4$@MoZn$_{22}$ heterostructures are obtained through decorating with a layer of MoZn$_{22}$ on the surface of CoMoO$_4$ samples (Fig. 3c). Uniform nanowall structures of the samples might exhibit large specific surface area. EDS mappings (Fig. 3d) shows that elements of Co, Mo, Zn and O are evenly distributed the whole sample, which is consistent of XPS analysis. Structural information of the CoMoO$_4$@MoZn$_{22}$ product is further investigated by TEM. Fig. 3e shows that a layer of MoZn$_{22}$ nanofilm is evenly coated on the surface of CoMoO$_4$ nanosheet. HRTEM image in Fig. 3f shows that two interplanar spacings of 0.208 nm and 0.213 nm correspond to the (4 2 2) plane of the CoMoO$_4$ phase and (1 1 4) plane of cubic MoZn$_{22}$, respectively.

The electrochemical performances of the as-synthesized products are investigated in three-electrode system using 3 M KOH aqueous solution as electrolyte. Fig. 4a–c show CV curves of CoMoO$_4$, MoZn$_{22}$ and CoMoO$_4$@MoZn$_{22}$ electrodes between a potential window varying from 0 to 0.65 V at a scan rate of 5–100 mV s^{-1}. With the increase of scan rate, CV curve area increases accordingly. Meanwhile, no significant change in the shapes of CV curves is observed, suggesting excellent structure stability of electrode materials. Fig. 4d–f exhibit GCD curves of the above mentioned electrodes at various current densities. Apparently, the charge and discharge time of the electrodes are almost the same, indicating the reversibility of the electrode materials.

CV curves of the as-synthesized electrode materials are recorded at a scan rate of 100 mV s^{-1} in different potential windows of 0–0.65 V (Fig. 5a). Since the specific capacitance of the electrode material is directly proportional to the area of the curve, CoMoO$_4$@MoZn$_{22}$ sample possesses the biggest area in three electrodes, indicating its superior specific capacitance to CoMoO$_4$ and MoZn$_{22}$ samples. The GCD curves of three electrode materials at 1 A g^{-1} are showed in Fig. 5b. It is observed that CoMoO$_4$@MoZn$_{22}$ electrodes present much longer discharge time than the other two electrodes. The specific capacitance of three-electrode material is a function of current density (Fig. 5c). The specific capacitance of CoMoO$_4$@MoZn$_{22}$ reaches 923 C g^{-1} at a current density of 1 A g^{-1}, and still retains 655 C g^{-1} when the current density increases 10 times. The capacitance retention is 71% when current density varies from 1 A g^{-1} to 10 A g^{-1}. In contrast, CoMoO$_4$

and MoZn$_{22}$ electrodes show capacitance retention of 56% and 54% at the same current density, respectively, indicating the excellent capacitive stability of CoMoO$_4$@MoZn$_{22}$ composites.

EIS of the electrode materials are studied in the frequency range from 100 kHz to 0.01 Hz at the amplitude of 0.01 V, as shown in Fig. 5d. The intercept of CoMoO$_4$@MoZn$_{22}$, CoMoO$_4$ and MnZn$_{22}$ electrode materials with X axis are 0.6, 1.1 and 0.8 Ω, respectively, revealing good conductivity and very low internal resistance of composite material. Meanwhile, the curve of composite electrode possesses maximum slope, it means that the diffusion of redox species in the electrolyte can be reflected from the slope of EIS curve in low frequency range. The diffusion controlled and pseudo-capacitive contribution to the total stored charges of CoMoO$_4$@MoZn$_{22}$ electrode at different scan rates are shown in Fig. 5e. The estimated diffusion controlled charges are about 84.6% of the total charges storage at a scan rate of 5 mV s^{-1}, which are more than the pseudo-capacitive induced ones, indicating effective diffusion charge storage ability of CoMoO$_4$@MoZn$_{22}$ composites. With the scan rate increasing, the diffusion controlled contribution becomes increasingly fewer. The cycling stabilities of the electrode materials are tested by 7000 charge-discharge cycling at a high current density of 20 A g^{-1}. As shown in Fig. 5f, the capacitance retention of CoMoO$_4$@MoZn$_{22}$ composite is 92.3%, which is much higher than those of CoMoO$_4$ (73.8%) and MoZn$_{22}$ (75%).

To study their practical applications in energy storage devices, an ASC is constructed by using CoMoO$_4$@MoZn$_{22}$ composite as positive electrode and AC as negative electrode. Fig. 6a exhibits CV curves of CoMoO$_4$@MoZn$_{22}$ and AC electrode, it is found that the operating potentials are 0–0.65 and −1.0–0 V, respectively, revealing that the potentials of electrode materials could be adequately utilized. Fig. 6b shows CV curves of the as-assembled device with different voltage window from 1.1 to 1.6 V at a scan rate of 100 mV s^{-1}. The CV curves at scan rate from 5 to 100 mV s^{-1} with the voltage window of 0–1.6 V are shown in Fig. 6c. The CV curves keep similar shapes even when the scan rate reaches 100 mV s^{-1}. It indicates fast charge/discharge capability of ASC. Galvanostatic discharge measurements between from 0 to 1.52 V are tested at various current densities (Fig. 6d). At a current density of 1 A g^{-1}, the specific capacitance reaches 169.3 C g^{-1}, which is much larger than previously reports [15,16]. Fig. 6e shows that the capacitance retention of the device is 97% after 10,000 cycles, which indicates its excellent cycle performance. The inset in Fig. 6e is the XRD pattern of positive electrode. After cycling, the diffraction peaks of the
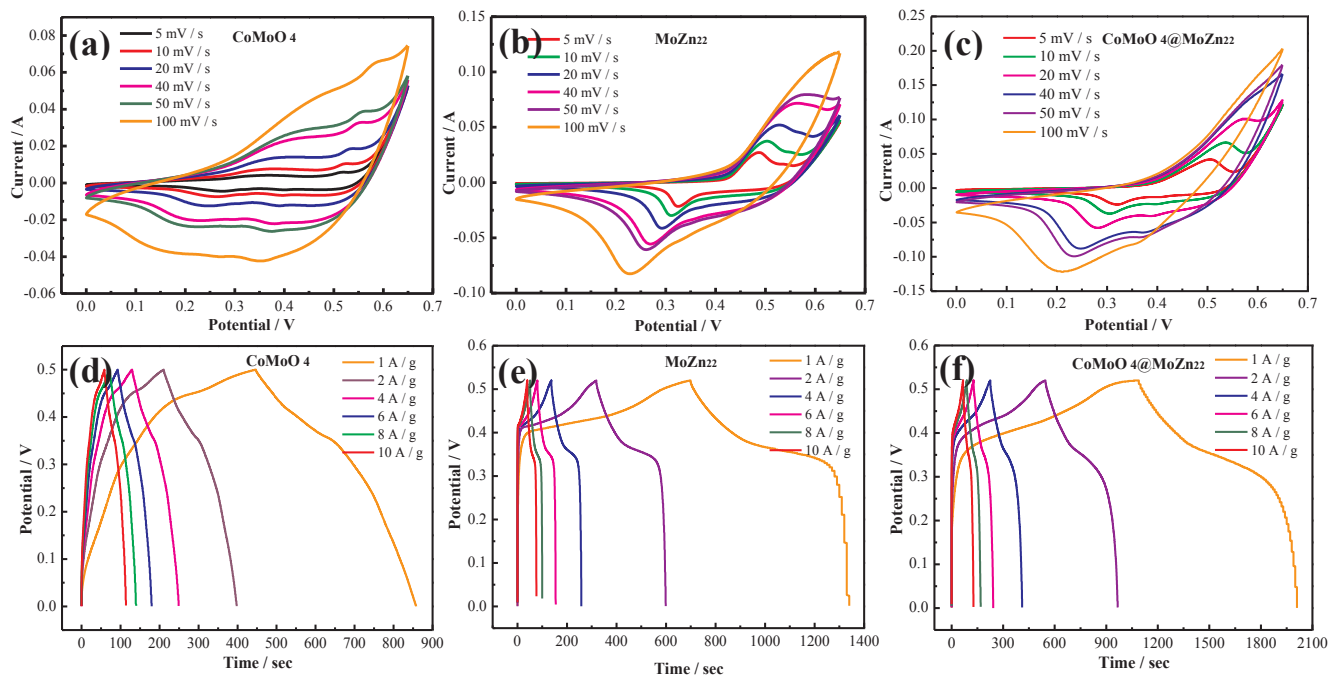
Fig. 4. (a–c) CV curves of three electrodes at scan rates 5–100 mV s^{-1} (d–f) GCD curves of three electrodes at different current densities.

electrode material shift to small angle, which might be ascribed to the fact that the ions in the electrolyte are accessible to the crystal lattice of electrode material and make the crystal cell increase. According to the charge/discharge curves at different current densities, the power densities and energy densities of CoMoO$_4$@MoZn$_{22}$//AC ASC are shown in Fig. 6f. It can deliver a maximum energy density of 129 Wh kg^{-1} at a power density of 2740 W kg^{-1}, which are superior to some previous reports [32,40–44].

In order to evaluate the electrocatalytic performances of electrode materials, OER activities are studied in 1 M KOH at a scan rate of 2 mV s^{-1}. Fig. 7a shows LSV curves of the as-synthesized electrodes. CoMoO$_4$@MoZn$_{22}$ electrode exhibits the larger current and lower overpotential (240 mV@20 mA cm^{-2}) than those of CoMoO$_4$ (260 mV@20 mA cm^{-2}) and MoZn$_{22}$ (295 mV@20 mA cm^{-2}). It indicates that a layer of MoZn$_{22}$ nanofilm possesses an excellent synergistic effect with CoMoO$_4$ nanosheets. Reaction kinetics of the electrocatalysts is further investigated by Tafel plots (Fig. 7b). The liner part of the Tafel plot is fitted by the following equation: η = a + b log j.
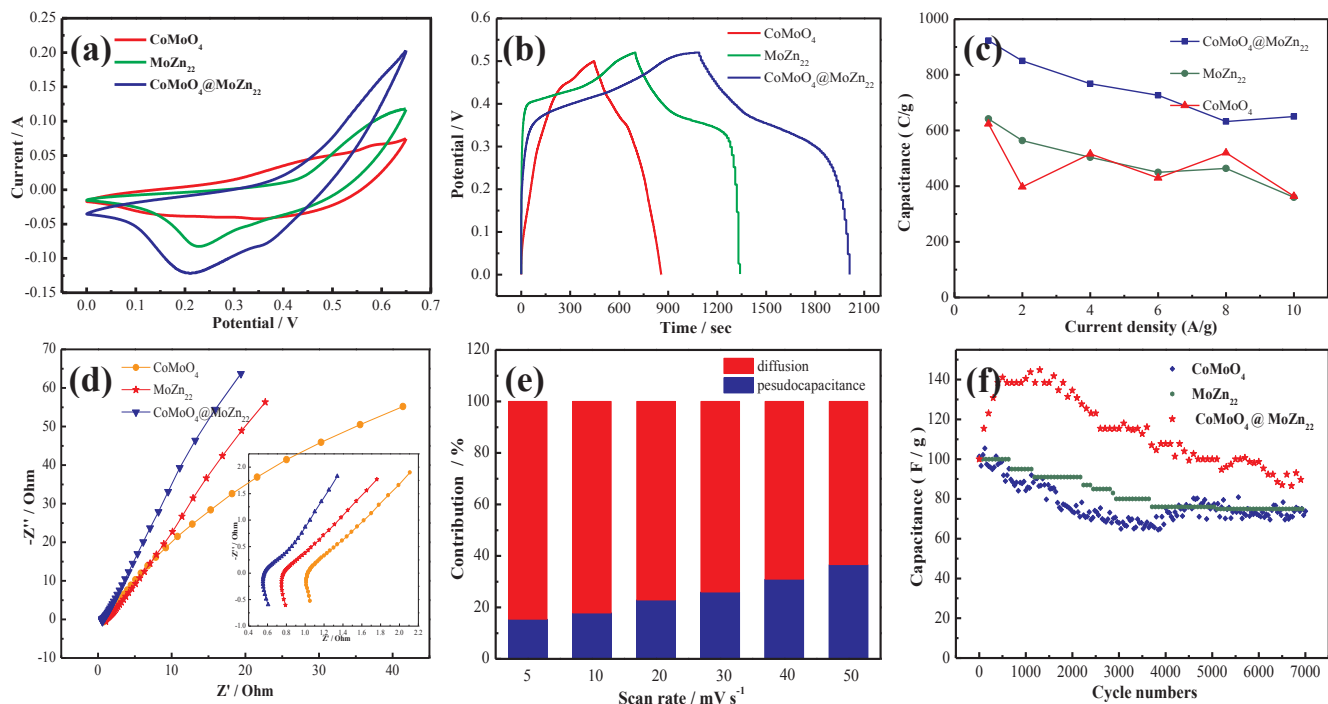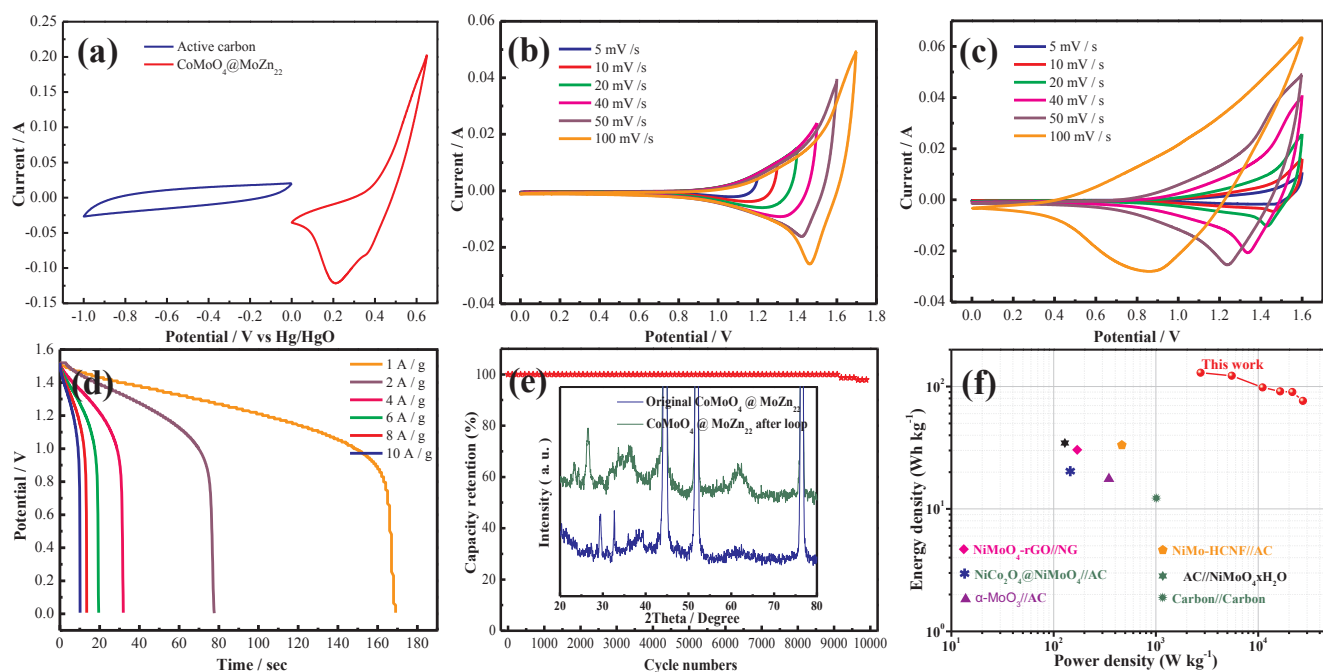

Fig. 5. Electrochemical characterizations of three electrodes (a) CV curves (b) GCD curves (c) Specific capacitances (d) Nyquist plots (e) Contribution ratio between capacitances and diffusion-limited ones (f) Cycling performance.

Fig. 6. Electrochemical characterizations of ASC (a) CV curves of active carbon and CoMoO₄@MoZn₂₂ (b) CV curves at different voltage windows (c) CV curves at different scan rates (d) GCD curves (e) Cycling performance, the inset shows the XRD patterns of composite materials before and after cycling (f) Ragone plots.
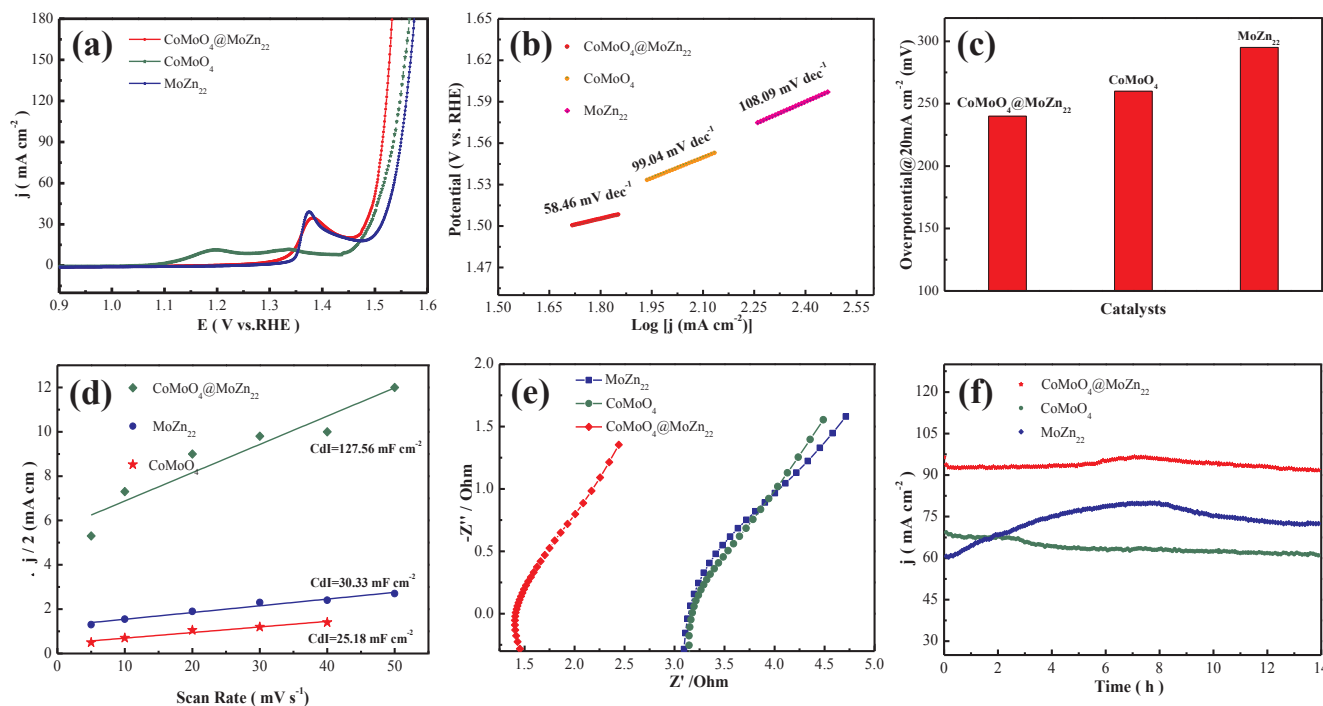
Fig. 7. Catalytic characterization (a) LSV curves (b) Tafel plots (c) overpotential of electrode materials (d) double-layered capacitance measurement linear fitting (e) Nyquist plots (f) stability tests.

Where η is the overpotential, b denotes Tafel slope and j represents current density. Tafel slopes of the electrode materials are 99.04 mV dec⁻¹, 108.09 mV dec⁻¹ and 58.46 mV dec⁻¹, respectively. In order to understand the reaction kinetics mechanism of electrocatalysts, electrochemically active surface area (ECSA) is studied by double layer capacitance (C$_{dl}$) at different scan rates from 0.1 to 0.3 V. As shown in Fig. 7d, C$_{dl}$ of CoMoO₄@MoZn₂₂ electrode material (127.56 mF cm⁻²) is higher than those of CoMoO₄ (28.18 mF cm⁻²) and MoZn₂₂ (30.33 mF cm⁻²). It demonstrates that high

electrochemical surface area of CoMoO₄@MoZn₂₂ might provide more active sites for OER. EIS of the electrodes in the frequency range of 0.01–100 kHz are shown in Fig. 7e, the R$_s$ value of CoMoO₄@MoZn₂₂, CoMoO₄ and MoZn₂₂ electrode materials are 1.48, 3.20 and 3.15 Ω, respectively. It suggests that the heterostructure benefits the exposure of the active sites, even improves OER performance. Fig. 7f shows cycle performances of the electrode materials, revealing excellent stability and not significant decrease after 14 h. It indicates that the as-prepared electrode materials possess excellent electrocatalytic performance.

Table 1

Electrochemical performance comparison of various electrode materials.

Materials	Specific capacitance	Current density	Electrolyte	Refs.
nanoporous Ni Alloy	$712\,C\,g^{-1}$ ($1424\,F\,g^{-1}$)	$1\,A\,g^{-1}$	4 M KOH	[20]
$CoMoO_4$ nanoflowers	$142\,C\,g^{-1}$ ($259\,F\,g^{-1}$)	$1\,A\,g^{-1}$	3 M KOH	[45]
WO_3 nanorods	$127\,C\,g^{-1}$ ($319.26\,F\,g^{-1}$)	$0.7\,A\,g^{-1}$	0.5 M H_2SO_4	[46]
$CoMoO_4$ nanosheets	$493\,C\,g^{-1}$ ($1234\,F\,g^{-1}$)	$1\,A\,g^{-1}$	3 M KOH	[47]
$MnCoO_4/CoMoO_4$ nanowires	$81\,C\,g^{-1}$ ($204.1\,F\,g^{-1}$)	$0.5\,A\,g^{-1}$	2 M NaOH	[48]
$NiCo_2O_4@CoMoO_4$ nanorods	$617\,C\,g^{-1}$ ($1543\,F\,g^{-1}$)	$1\,A\,g^{-1}$	2 M KOH	[49]
$CoMoO4@MoZn_{22}$ nanowalls	$923\,C\,g^{-1}$ ($1774\,F\,g^{-1}$)	$1\,A\,g^{-1}$	3 M KOH	This work

Table 2

Electrocatalytic performance comparison of various electrode materials.

Materials	η (mV)	Tafel (mV dec^{-1})	Cd (mF cm^{-2})	Refs.
Co-Fe Alloy nanofilm	290 (10 mA cm^{-2})	94	–	[50]
$CoMoO_4$ nanoarchitectures	286 (15 mA cm^{-2})	67	0.0702	[51]
$CoMoO_4$ porous flowers	312 (50 mA cm^{-2})	56	–	[33]
$MCo_2O_4@MCo_2S_4@ppy$ structures	298 (50 mA cm^{-2})	55.6	0.271	[2]
$CoMoO_4$ nanoneedle	343 (10 mA cm^{-2})	66	–	[52]
$CoMoO_4$ nanorods	343 (10 mA cm^{-2})	67	–	[32]
$CoMoO_4@MoZn_{22}$ nanowalls	240 (20 mA cm^{-2})	58.4	0.127	This work

Tables 1 and 2 illustrate the electrochemical performance of various electrode materials. The result shows that $CoMoO_4@MoZn_{22}$ electrode material possesses high specific capacitance and low overpotential [45–52].

4. Conclusion

In summary, bi-functional $CoMoO_4@MoZn_{22}$ electroactive materials are successfully grown on Ni foam via a facile hydrothermal route. It delivers outstanding specific capacitance and excellent cyclic performance. The as-assembled $CoMoO_4@MoZn_{22}$//AC ASC exhibits high energy density up to $129.4\,Wh\,kg^{-1}$ at a power density of $2740\,W\,kg^{-1}$ and 97% of its capacitance retention after 10,000 cycles. Meanwhile, the electrode material shows excellent performance for OER with a low overpotential. It demonstrates that this preparation strategy could be extended to synthesize other bi-functional electrode materials for energy storage and electrocatalysis.

Declaration of Competing Interest

The authors declare no conflict of interest

Acknowledgment

References

[1] B. Dunn, H. Kamath, J.M. Tarascon, Electrical energy storage for the grid: a battery of choices, Science 334 (2011) 928–935.

[2] D.P. Zhao, H.Q. Liu, X. Wu, Bi-interface induced multi-active $MCo_2O_4@MCo_2S_4@$ PPy (M = Ni, Zn) sandwich structure for energy storage and electrocatalysis, Nano Energy 57 (2019) 363–370.

[3] M. Wang, Y.P. Zhao, X.J. Zhang, R.J. Qi, S.S. Shi, Z.P. Li, Q.J. Wang, Y.F. Zhao, Interface-rich core-shell ammonium nickel cobalt phosphate for high-performance aqueous hybrid energy storage device without a depressed power density, Electrochim. Acta 272 (2018) 184–191.

[4] X. Wu, Z.C. Han, X. Zheng, S.Y. Yao, X. Yang, T.Y. Zhai, Core-shell structured $Co_3O4@NiCo_2O_2$ electrodes grown on flexible carbon fibers with superior electrochemical properties, Nano Energy 31 (2017) 410–417.

[5] J.K. Zhu, D.M. Song, T. Pu, J. Li, B. Huang, W.S. Wang, C.L. Zhao, L. Xie, L.Y. Chen, Two-dimensional porous $ZnCo_2O_4$ thin sheets assembled by 3D nanoflake array with enhanced performance for aqueous asymmetric supercapacitor, Chem. Eng. J. 336 (2018) 679–689.

[6] X. Wu, S.Y. Yao, Flexible electrode materials based on WO_3 nanotube bundles for high performance energy storage devices, Nano Energy 42 (2017) 143–150.

[7] S.L. Wang, W. Li, L.P. Xin, M. Wu, W.P. Sun, X.J. Lou, Pollen-inspired synthesis of porous and hollow NiO elliptical microstructures assembled from nanosheets for high-performance electrochemical energy storage, Chem. Eng. J. 321 (2017) 546–553.

[8] W. Jiang, F. Hu, Q.Y. Yan, X. Wu, Investigation on electrochemical behaviors of $NiCo_2O_4$ battery-type supercapacitor electrodes: the role of an aqueous electrolyte, Inorg. Chem. Front. 4 (2017) 1642–1648.

[9] H.Q. Liu, D.P. Zhao, P.F. Hu, X. Wu, Ternary core-shell structured transition metal chalcogenide for hybrid electrochemical capacitor, Chin. Chem. Lett. 29 (2018) 1799–1803.

[10] W.D. He, C.G. Wang, H.Q. Li, X.L. Deng, X.J. Xu, T.Y. Zhai, Ultrathin and porous $Ni_3S_2/CoNi_2S_4$ 3D network structure for superhigh energy density asymmetric supercapacitors, Adv. Energy Mater. 7 (2017) 1700983.

[11] C. Liu, X. Wu, $NiCo_2S_4$ nanotube arrays grown on flexible carbon fibers as battery-type electrodes for asymmetric supercapacitors, Mater. Res. Bull. 103 (2018) 55–62.

[12] L. Xu, Y. Zhao, J.B. Lian, Y.G. Xu, J. Bao, J.X. Qiu, L. Xu, H. Xu, M.Q. Hua, H.M. Li, Morphology controlled preparation of $ZnCo_2O_4$ nanostructures for asymmetric supercapacitor with ultrahigh energy density, Energy 123 (2017) 296–304.

[13] W. Jiang, F. Hu, S.Y. Yao, Z.P. Sun, X. Wu, Hierarchical $NiCo_2O_4$ nanowalls composed of ultrathin nanosheets as electrode materials for supercapacitor and Li ion battery applications, Mater. Res. Bull. 93 (2017) 303–309.

[14] W.X. Li, X.W. Wang, Y.C. Hu, L.Y. Sun, C. Gao, C.C. Zhang, H. Liu, M. Duan, Hydrothermal synthesized of $CoMoO_4$ microspheres as excellent electrode material for supercapacitor, Nanoscale Res. Lett. 13 (2018) 120.

[15] J. Wang, J. Chang, L. Wang, J. Hao, One-step and low-temperature synthesis of $CoMoO_4$ nanowire arrays on Ni foam for asymmetric supercapacitors, Ionics 24 (2018) 3967–3973.

[16] M. Li, S.H. Xu, C. Cherry, Y.P. Zhu, D.J. Wu, C. Zhang, X.L. Zhang, R. Huang, R.J. Qi, L.W. Wang, P.K. Chu, Hierarchical three dimensional $CoMoO_4$ nanoflakes on a macroporous electrically conductive network with superior electrochemical performance, J. Mater. Chem. A 3 (2015) 13776–13785.

[17] X. Zheng, Z.C. Han, S.Y. Yao, H.H. Xiao, F. Chai, F.Y. Qu, X. Wu, Spinous alpha-Fe_2O_3 hierarchical structures anchored on Ni foam for supercapacitor electrodes and visible light driven photocatalysts, Dalton Trans. 45 (2016) 7094–7103.

[18] J. Wang, X. Zhang, Q.L. Wei, H.M. Lv, Y.L. Tian, Z.Q. Tong, X.S. Liu, 3D self-supported nanopine forest-like $Co_3O_4@CoMoO_4$ core–shell architectures for high-energy solid state supercapacitors, Nano Energy 19 (2016) 222–234.

[19] H.H. Xiao, F.Y. Qu, X. Wu, Ultrathin NiO nanoflakes electrode materials for supercapacitors, Appl. Surf. Sci. 360 (2016) 8–13.

[20] S.W. Liu, Q. Zhao, M.Y. Tong, X.G. Zhu, G.Z. Wang, W.P. Cai, H.M. Zhang, H.J. Zhao, Ultrafine nickel-cobalt alloy nanoparticles incorporated into three-dimensional porous graphitic carbon as an electrode material for supercapacitors, J. Mater. Chem. A 4 (2016) 17080–17086.

[21] H.J. Xu, S.J. Pang, T. Zhang, Self-oxidized sponge-like nanoporous nickel alloy in three-dimensions with pseudocapacitive behavior and excellent capacitive performance, J. Power Sources 399 (2018) 192–198.

[22] P.R. Wu, C.L. Wu, D.H. Chen, Synthesis and controlled sulfidation of Ni-Co alloy on reduced graphene oxide as an electrode with enhanced conductivity and capacitance for supercapacitors, J. Alloys Compd. 735 (2018) 409–416.

[23] W. Li, S.L. Wang, M. Wu, X.J. Wang, Y. Long, X.J. Lou, Direct aqueous solution synthesis of an ultra-fine amorphous nickel-boron alloy with superior pseudocapacitive performance for advanced asymmetric supercapacitors, New J. Chem. 41 (2017) 7302–7311.

[24] D.F. Yan, Y.X. Li, J. Huo, R. Chen, L.M. Dai, S.Y. Wang, Defect chemistry of

nonprecious-metal electrocatalysts for oxygen reactions, Adv. Mater. 29 (2017) 1606459.

[25] X.D. Jia, Y.F. Zhao, G.B. Chen, L. Shang, R. Shi, X.F. Kang, G. Waterhouse, L.Z. Wu, C.H. Tung, T.R. Zhang, Ni₃FeN nanoparticles derived from ultrathin NiFe-layered double hydroxide nanosheets: an efficient overall water splitting electrocatalyst, Adv. Energy Mater. 6 (2016) 1502585.

[26] L.S. Xie, X. Ren, Q. Liu, G.W. Cui, R.X. Ge, A.M. Asiri, X.P. Sun, Q.J. Zhang, L. Chen, A Ni(OH)(2)-PtO₂ hybrid nanosheet array with ultralow Pt loading toward efficient and durable alkaline hydrogen evolution, J. Mater. Chem. A 6 (2018) 1967–1970.

[27] X.Y. Lu, C.A. Zhao, Electrodeposition of hierarchically structured three dimensional nickel-iron electrodes for efficient oxygen evolution at high current densities, Nat. Commun. 6 (2015) 6616.

[28] V. Petrykin, K. Macounova, O.A. Shlyakhtin, P. Krtil, Tailoring the selectivity for electrocatalytic oxygen evolution on ruthenium oxides by zinc substitution, Angew. Chem. Int. Ed. 49 (2010) 4813–4815.

[29] Y. Lee, J. Suntivich, K.J. May, E.E. Perry, Y. Shao-Horn, Synthesis and activities of rutile IrO₂ and RuO₂ nanoparticles for oxygen evolution in acid and alkaline solutions, J. Phys. Chem. Lett. 3 (2012) 399–404.

[30] C.Z. Yuan, L. Yang, L.R. Hou, L.F. Shen, X.G. Zhang, X.W. Lou, Growth of ultrathin mesoporous Co₃O₄ nanosheet arrays on Ni foam for high-performance electrochemical capacitors, Energy Environ. Sci. 5 (2012) 7883–7887.

[31] C. Guan, J.P. Liu, C.W. Cheng, H.X. Li, X.L. Li, W.W. Zhou, H. Zhang, H.J. Fan, Hybrid structure of cobalt monoxide nanowire@nickel hydroxidenitrate nanoflake aligned on nickel foam for high-rate supercapacitor, Energy Environ. Sci. 4 (2011) 4496–4499.

[32] D. Cheng, Y.F. Yang, J.L. Xie, C.J. Fang, G.Q. Zhang, J. Xiong, Hierarchical NiCo₂O₄@NiMoO₄ core-shell hybrid nanowire/nanosheet arrays for high-performance pseudocapacitors, J. Mater. Chem. A 3 (2015) 14348–14357.

[33] X.L. Liu, Y.X. Yang, S.Y. Guan, An efficient electrode based on one-dimensional CoMoO₄ nanorods for oxygen evolution reaction, Chem. Phys. Lett. 675 (2017) 11–14.

[34] M.Q. Yu, L.X. Jiang, H.G. Yang, Ultrathin nanosheets constructed CoMoO₄ porous flowers with high activity for electrocatalytic oxygen evolution, Chem. Comm. 51 (2015) 14361–14364.

[35] D. Hou, S.Y. Zhu, H. Tian, H. Wei, X.L. Feng, Y.Y. Mai, Two-dimensional sandwich-structured mesoporous Mo₂C/carbon/graphene nanohybrids for efficient hydrogen production electrocatalysts, ACS Appl. Mater. Interfaces 10 (2018) 40800–40807.

[36] D.P. Zhao, M.Z. Dai, H.Q. Liu, L. Xiao, X. Wu, H. Xia, Constructing high performance hybrid battery and electrocatalyst by heterostructured NiCo₂O₄@NiWS nanosheets, Cryst. Growth Des. 19 (2019) 1921–1929.

[37] R. Chen, C.J. Yang, W.Z. Cai, H.Y. Wang, J.W. Miao, L.P. Zhang, S.L. Chen, B. Liu, Use of Platinum as the counter electrode to study the activity of nonprecious metal catalysts for the hydrogen evolution reaction, ACS Energy Lett. 2 (2017) 1070–1075.

[38] F.L. Wu, Q.L. Liao, F.R. Cao, L. Li, Y. Zhang, Non-noble bimetallic NiMoO₄

[39] L.L. Hu, B.H. Qu, C.C. Li, Y.J. Chen, L. Mei, D.N. Lei, L.B. Chen, Q.H. Li, T.H. Wang, Facile synthesis of uniform mesoporous ZnCo₂O₄ microspheres as a high-performance anode material for Li-ion batteries, J. Mater. Chem. A 1 (2013) 5596–5602.

[40] T. Liu, H. Chai, D. Jia, Y. Su, T. Wang, W.Y. Zhou, Rapid microwave-assisted synthesis of mesoporous NiMoO₄ nanorod/reduced graphene oxide composites for high-performance supercapacitors, Electrochim. Acta 180 (2015) 998–1006.

[41] F. Barzegar, A. Bello, D.Y. Momodu, J.K. Dangbegnon, F. Taghizadeh, M.J. Madito, T.M. Masikhwa, N. Manyala, Asymmetric supercapacitor based on an alpha-MoO₃ cathode and porous activated carbon anode materials, RSC Adv. 5 (2015) 37462–37468.

[42] V.S. Budhiraju, R. Kumar, A. Sharma, S. Sivakumar, Structurally stable hollow mesoporous graphitized carbon nanofibers embedded with NiMoO₄ nanoparticles for high performance asymmetric supercapacitors, Electrochim. Acta 238 (2017) 337–348.

[43] M.C. Liu, L. Kang, L.B. Kong, C. Lu, X.J. Ma, X.M. Li, Y.C. Luo, Facile synthesis of NiMoO₄ center dot xH(2)O nanorods as a positive electrode material for supercapacitors, RSC Adv. 3 (2013) 6472–6478.

[44] B. Liu, Y.J. Liu, H.B. Chen, M. Yang, H.M. Li, Oxygen and nitrogen co-doped porous carbon nanosheets derived from Perilla frutescens for high volumetric performance supercapacitors, J. Power Sources 341 (2017) 309–317.

[45] J. Candler, T. Elmore, B.K. Gupta, L.F. Dong, S. Palchoudhury, R.K. Gupta, New insight into high-temperature driven morphology reliant CoMoO₄ flexible supercapacitors, New J. Chem. 39 (2015) 6108–6116.

[46] S.Y. Yao, F.Y. Qu, G. Wang, X. Wu, Facile hydrothermal synthesis of WO₃ nanorods for photocatalysts and supercapacitors, J. Alloys Compd. 724 (2017) 695–702.

[47] H.W. Long, T.M. Liu, W. Zeng, Y.F. Yang, S.Q. Zhao, CoMoO₄ nanosheets assembled 3D-frameworks for high-performance energy storage, Ceram. Int. 44 (2018) 2446–2452.

[48] L.Q. Mai, F. Yang, Y.L. Zhao, X. Xu, L. Xu, Y.Z. Luo, Hierarchical MnMoO₄/CoMoO₄ heterostructured nanowires with enhanced supercapacitor performance, Nat. Commun. 2 (2011) 381.

[49] X.W. Dong, Y.Y. Zhang, W.J. Wang, R. Zhao, Rational construction of 3D NiCo₂O₄@CoMoO₄ core/shell nanoarrays as a positive electrode for asymmetric supercapacitor, J. Alloys Compd. 729 (2017) 716–723.

[50] A. Samanta, C.R. Raj, Catalyst support in oxygen electrocatalysis: a case study with CoFe alloy electrocatalyst, J. Phys. Chem. C 122 (2018) 15843–15852.

[51] F.F. Wang, J. Zhao, W. Tian, Z.F. Hu, X.B. Lv, H.L. Zhang, H.R. Yue, Y.X. Zhang, J.Y. Ji, W. Jiang, Morphology-controlled synthesis of CoMoO₄ nanoarchitectures anchored on carbon cloth for high-efficiency oxygen oxidation reaction, RSC Adv. 9 (2019) 1562–1569.

[52] L.X. Fang, F. Wang, T.L. Zhai, Y. Qiu, M.D. Lan, K.J. Huang, Q.S. Jing, Hierarchical CoMoO₄ nanoneedle electrodes for advanced supercapacitors and electrocatalytic oxygen evolution, Electrochim. Acta 259 (2018) 552–558.